

Contents lists available at [ScienceDirect](http://ScienceDirect)

# Earth and Planetary Science Letters

[www.elsevier.com/locate/epsl](http://www.elsevier.com/locate/epsl)


## Fe-XANES analyses of Reykjanes Ridge basalts: Implications for oceanic crust's role in the solid Earth oxygen cycle



Oliver Shorttle<sup>a,\*</sup>, Yves Moussallam<sup>a</sup>, Margaret E. Hartley<sup>a</sup>, John Maclennan<sup>a</sup>, Marie Edmonds<sup>a</sup>, Bramley J. Murton<sup>b</sup>

<sup>a</sup> Department of Earth Sciences, University of Cambridge, Downing Street, Cambridge CB2 3EQ, UK

<sup>b</sup> National Oceanography Centre, University of Southampton, Waterfront Campus, European Way, Southampton, SO14 3ZH, UK

### ARTICLE INFO

#### Article history:

Received 16 March 2015

Received in revised form 8 July 2015

Accepted 10 July 2015

Available online 25 July 2015

Editor: T.A. Mather

#### Keywords:

mantle  $f_{O_2}$

XANES

oxygen

mantle heterogeneity

pyroxenite

### ABSTRACT

The cycling of material from Earth's surface environment into its interior can couple mantle oxidation state to the evolution of the oceans and atmosphere. A major uncertainty in this exchange is whether altered oceanic crust entering subduction zones can carry the oxidised signal it inherits during alteration at the ridge into the deep mantle for long-term storage. Recycled oceanic crust may be entrained into mantle upwellings and melt under ocean islands, creating the potential for basalt chemistry to constrain solid Earth–hydrosphere redox coupling.

Numerous independent observations suggest that Iceland contains a significant recycled oceanic crustal component, making it an ideal locality to investigate links between redox proxies and geochemical indices of enrichment. We have interrogated the elemental, isotope and redox geochemistry of basalts from the Reykjanes Ridge, which forms a 700 km transect of the Iceland plume. Over this distance, geophysical and geochemical tracers of plume influence vary dramatically, with the basalts recording both long- and short-wavelength heterogeneity in the Iceland plume. We present new high-precision Fe-XANES measurements of  $Fe^{3+}/\sum Fe$  on a suite of 64 basalt glasses from the Reykjanes Ridge. These basalts exhibit positive correlations between  $Fe^{3+}/\sum Fe$  and trace element and isotopic signals of enrichment, and become progressively oxidised towards Iceland: fractionation-corrected  $Fe^{3+}/\sum Fe$  increases by  $\sim 0.015$  and  $\Delta QFM$  by  $\sim 0.2$  log units. We rule out a role for sulfur degassing in creating this trend, and by considering various redox melting processes and metasomatic source enrichment mechanisms, conclude that an intrinsically oxidised component within the Icelandic mantle is required. Given the previous evidence for entrained oceanic crustal material within the Iceland plume, we consider this the most plausible carrier of the oxidised signal.

To determine the ferric iron content of the recycled component ( $[Fe_2O_3]_{source}$ ) we project observed liquid compositions to an estimate of  $Fe_2O_3$  in the pure enriched endmember melt, and then apply simple fractional melting models, considering lherzolitic and pyroxenitic source mineralogies, to estimate  $[Fe_2O_3]_{source}$  content. Propagating uncertainty through these steps, we obtain a range of  $[Fe_2O_3]_{source}$  for the enriched melts (0.9–1.4 wt%) that is significantly greater than the ferric iron content of typical upper mantle lherzolites. This range of ferric iron contents is consistent with a hybridised lherzolite–basalt (pyroxenite) mantle component. The oxidised signal in enriched Icelandic basalts is therefore potential evidence for seafloor–hydrosphere interaction having oxidised ancient mid-ocean ridge crust, generating a return flux of oxygen into the deep mantle.

© 2015 The Authors. Published by Elsevier B.V. This is an open access article under the CC BY license (<http://creativecommons.org/licenses/by/4.0/>).

### 1. Introduction

The movement of oxygen between the surface and subsurface of the planet has played a key role in the compositional and physical evolution of all terrestrial reservoirs (Frost, 1991). One means of reconstructing past oxygen fluxes is from mantle rocks, which

can preserve chemical signals of ancient and modern redox processes through subduction recycling. Models of the modern surface oxygen budget emphasise the role of oceanic crust as a long-term sink for oxygen via seawater sulfate reduction during hydrothermal processes at ridges (Lécuyer and Ricard, 1999; Sleep, 2005). This oxygen is bound into the oceanic crust as ferric iron ( $Fe_2O_3$ ) and returned to the mantle during subduction, where it may enter into the mantle's convective circulation, or be rapidly extracted at subduction zones (Kelley and Cottrell, 2009). If subduc-

\* Corresponding author.

E-mail address: [os258@cam.ac.uk](mailto:os258@cam.ac.uk) (O. Shorttle, B. Murton).

tion has transported oxygen from the hydrosphere into the deep Earth then basalts sampling trace element-enriched mantle domains, which are commonly attributed to ancient recycled oceanic crust (Chase, 1981; Stracke, 2012), should be oxidised relative to basalts sampling ambient mantle (Carmichael, 1991; Lécuyer and Ricard, 1999). However, a prediction that all enriched mantle domains sample oxidised slabs is inconsistent with the recent finding that some enriched mantle domains, far from plumes, are more reduced than ambient mantle (Cottrell and Kelley, 2013). Here we investigate the role of enriched mantle domains in solid Earth redox cycling, with a focused regional study of the  $\text{Fe}_2\text{O}_3$  content of plume-influenced mid-ocean ridge basalts around Iceland.

We have made new high-precision determinations of the proportion of ferric iron, expressed as  $\text{Fe}^{3+}/\sum\text{Fe}$ , by X-ray absorption near edge structure (XANES) spectroscopy in 64 basalt glasses from the Reykjanes Ridge south of Iceland (Murton, 1995; Murton et al., 2002). Compositional variability in these samples offers the potential to probe the oxidation state of enriched and depleted mantle domains on the broad scale of the Iceland swell and geochemical anomaly (Schilling, 1973), as well as the short length-scale of single enriched seamounts. We begin with a description of the XANES methods we have used to obtain our new dataset. In particular we show that detailed time-resolved observations of the pre-edge structure can rule out beam damage oxidising the iron in natural basalt samples. We then discuss these observations in the context of degassing, crystallisation and melting processes. We remove the effect of crystallisation and rule out degassing as a significant control on the oxidation state of most Reykjanes Ridge basalts. Finally, we relate the  $\text{Fe}_2\text{O}_3$  data to a model of oceanic crustal recycling and the reintroduction of oxidised material to the mantle.

## 2. XANES methods

### 2.1. Spectral acquisition

Samples were analysed on the I18 beamline at Diamond Light Source (DLS) to probe the detailed pre-edge structure of the Fe K-edge with synchrotron X-rays over the energy range 7020–7500 eV. The X-ray beam was monochromatised using a double Si(333) crystal. The energy step sizes and dwell times used are given in Table A.1. The beam dimensions were  $5\times 3\ \mu\text{m}^2$ , and the experimental geometry had the sample at  $45^\circ$  to the incident X-ray beam and  $45^\circ$  from the collector, giving an incident-fluoresced X-ray angle of  $90^\circ$ . Incident X-ray intensity was measured using a 1.5 cm long ionisation chamber, and the intensity of fluoresced X-rays were measured using a four element silicon drift detector.

Almost all analyses were performed during a single four-day analytical session in August 2014. Sample 98D3, and repeat analyses of 183D2 and 174D9, were performed one month later in a separate session. During our main analytical session the storage ring was operating at 3 GeV with an electron current of 300 mA. For the second session, operating conditions at the beamline had changed: the electron current was now 200 mA and we used a germanium detector with nine elements. In all analyses, attenuation of the primary X-ray beam by 0.1 mm Al plates was employed to keep the count rate below the saturation limit of the detector. These analytical conditions translate into a photon flux of  $\sim 10^9$  photons/s.

### 2.2. Beam damage

Beam damage has been reported during sulfur XANES analyses, where the effect has been to oxidise sulfur over minutes (Wilke et al., 2008; Métrich et al., 2009; Moussallam et al., 2014).

A systematic investigation of whether the long-term exposure of basaltic samples to a  $\mu$ -XANES X-ray beam can cause Fe oxidation/reduction was carried out by Cottrell and Kelley (2009) at the National Synchrotron Light Source (USA). The Cottrell and Kelley (2009) study found no spectral shift resulting from repeated and extended sample exposure to the X-ray beam (using cumulative exposure times at least twice as great as our 30-min analyses). At DLS, Moussallam et al. (2014) acquired multiple XANES spectra on the same spot to test whether there was a progressive beam damage effect for Fe, but saw no change in Fe oxidation state despite significant changes in S oxidation. These results imply that Fe is more stable than S during XANES analysis of silicate glasses.

To establish whether beam damage was occurring we performed an additional test using the natural basalt 153D3 from our sample set (0.17 wt%  $\text{H}_2\text{O}$ , typical of Reykjanes Ridge basalts, Nichols et al., 2002). The test consisted of positioning the monochromator at a fixed energy of 7114.3 eV, corresponding to the oxidised peak of the pre-edge doublet. Before allowing the beam to illuminate the sample we began collecting the fluoresced X-rays in 1 s time windows, then opened the shutter on the sample. This experiment tested the hypothesis that beam damage was occurring rapidly during the initial exposure of the sample to the beam: if beam damage was taking place we should have seen a large drift in the fluoresced X-ray count towards higher values if the beam damage was oxidative, or towards lower values if the damage was reductive. Instead, with the same analytical conditions as for our measurements of natural samples, we found that no drift in energy occurs at the onset, or thereafter, of the sample being exposed to the beam (Fig. 1A and B). This result indicates that Fe in our samples was neither oxidised nor reduced during the XANES analyses.

We did find that changing the analytical conditions by removing the Al attenuators was able to generate a very small amount of photo-oxidation over the first 700 s of exposure of the sample to the beam (Fig. 1C). However, even this amount of photo-oxidation is over two orders of magnitude less than the natural variability the samples exhibit, and is barely above the instrument stability. Furthermore, that we can see slight photo oxidation under the particular circumstances where the beam is not attenuated, gives us confidence that no photo-oxidation is occurring when we don't see this signal using an attenuated beam.

### 2.3. Processing of spectra

As has been noted previously (Berry et al., 2003; Farges et al., 2004; Cottrell and Kelley, 2009) the handling of the raw XANES spectra can have a significant influence on the  $\text{Fe}^{3+}/\sum\text{Fe}$  calculated for the unknown materials, which although less significant for a relative study, has the potential to systematically offset the results produced by different groups. To mitigate against this problem we provide a detailed description of the calibration procedure we have selected and include in the supplementary material the normalised spectra we collected so that future comparisons between datasets can be carried out in a self-consistent manner.

The first derivative peak on an Fe foil, 7112.0 eV, measured at the start of the analytical session, provided the energy calibration for the spectra. Following the method of Wilke et al. (2001) a Victoreen function

$$v_1 F^3 + v_2 F^4, \quad (1)$$

was fit to the region 7020–7090 eV before the pre-edge, where  $F = I_f/I_0$  is the ratio of fluoresced to incident X-rays and  $v_1$  and  $v_2$  are the parameters to be optimised. The Levenberg–Marquardt optimisation algorithm (Press et al., 1992) was used to find the best fitting parameters. The Victoreen function was subtracted from the spectra, which was then normalised to an edge-step of

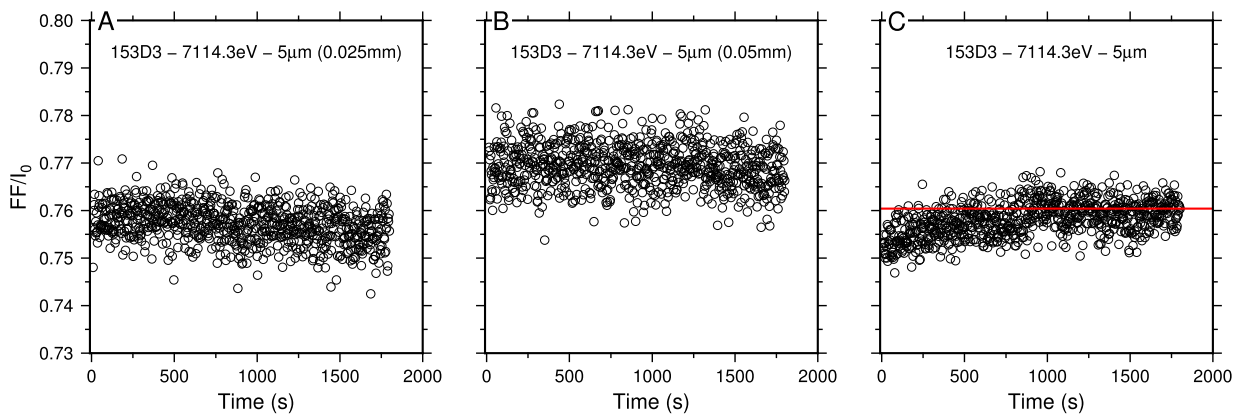


**Fig. 1.** Time series of  $I_0$  normalised fluoresced intensity (FF) at 7114.3 eV, the energy of the oxidised peak of the pre-edge doublet. This test was performed to determine whether there was time-dependent sample damage from exposure to the high energy X-ray beam. The test used the same beam conditions as our analyses of natural Reykjanes Ridge basalts, and was performed on sample 153D3. A fresh spot on the sample was illuminated with a 5  $\mu\text{m}$  diameter beam and the fluoresced intensity integrated over 1 s intervals. Plots A–C record, respectively, the time series produced for illumination from a beam attenuated with a 0.025 mm Al plate, 0.05 mm Al plate, and with no attenuation. In C, the red line marks the FF/ $I_0$  at 7114.3 eV from a subsequent full spectrum acquisition ( $\sim 30$  min). (For interpretation of the references to colour in this figure legend, the reader is referred to the web version of this article.)

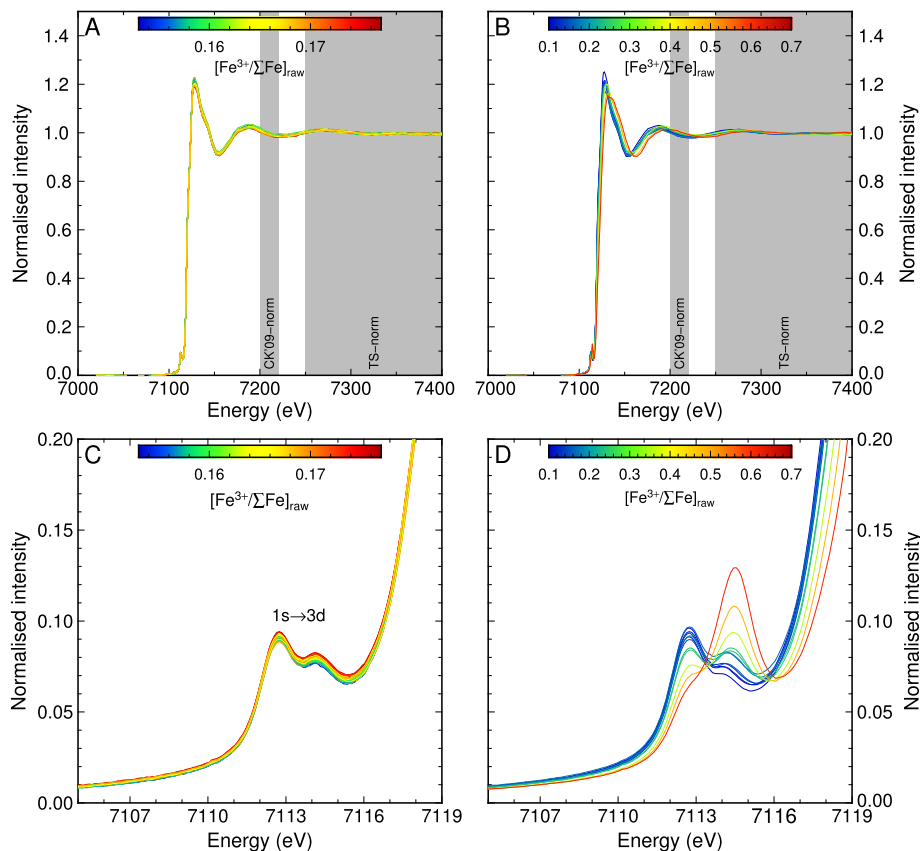


**Fig. 2.** Edge-step normalised intensity vs. energy for sample and reference spectra. (A) and (B) show the full spectra collected from samples and standards (NMNH 117393, Cottrell and Kelley, 2009) respectively, with the energy range used in this study for normalisation marked on as the grey band ‘TS-norm’ and the energy range used by Cottrell and Kelley (2009) marked on as ‘CK’09-norm’. Spectra have been coloured by their  $\text{Fe}^{3+}/\sum\text{Fe}$  as determined from the XANES analyses (in the case of the reference glasses, this  $\text{Fe}^{3+}/\sum\text{Fe}$  is effectively the reference value as determined by Mössbauer). (C) and (D) show spectra over the energy range of the pre-edge region we used in fitting the spectra from the samples and standards respectively. Over the pre-edge region, counting times were 5–10 s and energy steps were 0.1 eV.

1 by taking the average intensity over the region 7250–7400 eV. This energy range was chosen in order to avoid incorporating the highest amplitude oscillation of the post-edge spectrum, which itself moves as a function of  $\text{Fe}^{3+}/\sum\text{Fe}$  (see for example Fig. 2B), potentially making the normalisation sensitive to the sample’s oxidation state.

The results of this normalisation routine can be seen in Fig. 2, in which the normalised spectra for samples and reference glasses are plotted.

#### 2.4. Calibration of spectra for $\text{Fe}^{3+}/\sum\text{Fe}$

We used the NMNH 117393 basalt reference block made by Cottrell and Kelley (2009), and loaned by the Smithsonian Institution National Museum of Natural History, to calibrate  $\text{Fe}^{3+}/\sum\text{Fe}$  in the unknown sample spectra.

A common method for determining the  $\text{Fe}^{3+}/\sum\text{Fe}$  ratio of a material is to use the energy of the  $1s \rightarrow 3d$  pre-edge transition, which forms an absorption multiplet prior to the main Fe K-edge

(Fig. 2C). The  $1s \rightarrow 3d$  pre-edge feature shifts to higher energy and the relative height of its peak changes as  $\text{Fe}^{3+}/\sum\text{Fe}$  increases (e.g. Wong et al., 1984; Bajt et al., 1994 and Fig. 2D), meaning that it can be used to calibrate for  $\text{Fe}^{3+}/\sum\text{Fe}$  in unknowns. A majority of techniques for quantifying the pre-edge feature are ‘function fitting’ methods, in which a combination of functions are fit to some range of the pre-edge region (between 7100–7120 eV) in order to extract a single parameter (such as centroid energy or peak height ratio) that can be related to  $\text{Fe}^{3+}/\sum\text{Fe}$  (Berry et al., 2003). Often these routines combine two families of functions; one set designed to remove the ‘background’ associated with the main absorption edge, whilst the second set fits the smaller amplitude pre-edge feature.

However, it is apparent from Fig. 2D that it is not only the  $1s \rightarrow 3d$  pre-edge feature that responds to increasing  $\text{Fe}^{3+}/\sum\text{Fe}$  in the glass. The rise to the main absorption edge also moves to higher energy, by up to  $\sim 1$  eV for the range of oxidation states represented in the NMNH 117393 glasses. This is valuable extra information that could potentially be incorporated into forming a calibration for  $\text{Fe}^{3+}/\sum\text{Fe}$  (Berry et al., 2003). Using information beyond simply the position of the  $1s \rightarrow 3d$  multiplet would be especially useful for natural mid-ocean ridge basalt (MORB) samples, in which the absolute variability of  $\text{Fe}^{3+}/\sum\text{Fe}$  so far reported by XANES is extremely limited ( $\sim 3\%$ , Cottrell and Kelley, 2011, 2013).

In order to maximise the amount of information we use in calibrating the unknown spectra for  $\text{Fe}^{3+}/\sum\text{Fe}$ , and thereby increase the signal to noise, we have used principal component regression (PCR). PCR is a linear mixing method (e.g. Manceau et al., 1992; Farges et al., 2004) which first identifies spectral features corresponding to the maximum variance in the dataset through conventional principal component analysis (PCA). For the reference spectra with known  $\text{Fe}^{3+}/\sum\text{Fe}$ , these components can then be linearly correlated with  $\text{Fe}^{3+}/\sum\text{Fe}$  to produce a simple linear mixing model able to predict  $\text{Fe}^{3+}/\sum\text{Fe}$  (Malherbe and Claverie, 2013; Vigneau et al., 1997). All that is required is that the PCA be performed simultaneously on the samples and standards so that the principal components form a common basis for each dataset. A decision still has to be made about how much of the spectrum to include to optimise the analysis, with practical limitations on analysis time meaning that we have here included only the pre-edge region (7105–7119 eV) for which we have the highest quality data (Table A.1). However, PCR is readily extensible to all parts of the spectrum that are thought to contain information on oxidation state – with components describing effects uncorrelated with valence changes (such as noise) readily identified from the statistical insignificance of their associated parameters in the mixing model.

The result of the initial PCA for our combined dataset of sample and standard spectra is shown in Fig. 3 for the region 7105–7119 eV, which is useful as a visual description of why the PCR method works. Principal component 1 (PC1) effectively describes an average of the spectra studied which, given the abundance of sample spectra (64) compared to reference spectra (12), is relatively reduced (compare with spectra in Fig. 2B). Although PC1 describes a majority of the variance (99.6%), additional components are required to describe the systematic shifts in the pre-edge multiplet occurring with changing oxidation state. The component that most clearly creates the expected shifts in the pre-edge is PC2, which describes a peak at  $\sim 7114.5$  eV that, when mixed with PC1, shifts the relative amplitude of the pre-edge multiplet to higher or lower energies. Taking a linear mixture of PC1 and PC2 is thus similar to the process of fitting the pre-edge with the Gaussian, Lorentzian and pseudo-Voigt functions of other calibration methods; however, PCA allows the data to define the best fitting form for the peaks, and no information is discarded as background.

Principal component analysis also offers a useful check of whether the reference spectra exhibit the same structural features

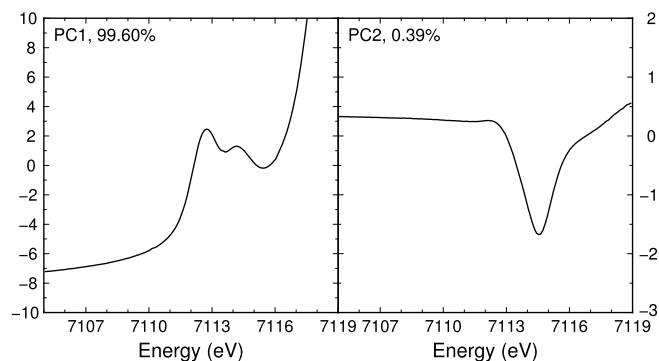


**Fig. 3.** Projection of the first two principal components (PC1 and PC2) into energy space, showing how the principal components combine to reproduce the pre-edge structure of the sample and standard spectra. PC1 effectively represents an average spectrum which, because of the larger number of samples compared with standards, exhibits the spectral features of the  $1s\text{--}3d$  transition in a glass with  $\text{Fe}^{3+}/\sum\text{Fe} \sim 0.15$ , i.e. roughly the ferric iron content of the natural glasses in our study. The second principal component consists of a peak at  $\sim 7114.5$  eV that, when mixed in with PC1, can add to or subtract from the second peak in PC1, creating the pre-edge structure of the more oxidising reference glasses (compare with Fig. 2D). In contrast, higher components begin to show dominantly high frequency structure indicating that they are largely mapping noise.

as the unknowns, similar to using the pre-edge intensity and centroid energy (Wilke et al., 2001). This is particularly important given the potential for Fe coordination to influence the pre-edge structure of the spectra and for these structural effects to vary between natural and synthetic materials. We show the first two PCs from our dataset in Fig. 4. The overlap in PC1 and PC2 between the sample and reference spectra, combined with their similarity in centroid position and pre-edge intensity, is good evidence that the pre-edge structure in both sets of materials is varying in response to the same process: in this case the ratio  $\text{Fe}^{3+}/\sum\text{Fe}$ .

After PCA, the next step is to perform the multiple linear regression of the selected PCs as predictors of  $\text{Fe}^{3+}/\sum\text{Fe}$ . To do this we have used the ‘ols’ function from the ‘rms’ package in the R statistical programming language (R Core Team, 2013), which carries out weighted ordinary least squares regression. We have used both PC1 and PC2 so as to incorporate information on the whole pre-edge region into the calibration. Applying this method, the form of the calibration to  $\text{Fe}^{3+}/\sum\text{Fe}$  is:

$$\text{Fe}^{3+}/\sum\text{Fe} = a_0 + a_1\text{PC1} + a_2\text{PC2}, \quad (2)$$

where  $a_0$ ,  $a_1$  &  $a_2$  are the regression coefficients, and PC1 and PC2 the principal component scores for the spectra. We note that PC1 and PC2 could also have higher degree terms included in this equation; however, the improvement in fit from including these additional terms is not significant and does not change our results.

The multiple linear regression using both PC1 and PC2 is shown in Fig. A.1. The reduced chi-squared for this fit is 2.3, and remains almost constant if three or more components are used, indicating that the calibration performs reasonably with just the first two components.

### 2.5. Precision

Over our analytical session we made four repeat analyses of the suite of NMNH 117393 reference glasses. In the final PCR calibration we used an average spectrum for each reference glass. However, we can also take each set of NMNH 117393 analyses separately and use these to calibrate the data for  $\text{Fe}^{3+}/\sum\text{Fe}$ . This acts as a test of the calibration’s intra-session drift and stability. Recalibrating the data there is no evidence of drift within the session, nor significant variability depending upon the set of standard analyses chosen to perform the calibration (see supplementary information). The  $1\sigma$  precision calculated on  $\text{Fe}^{3+}/\sum\text{Fe}$  from the

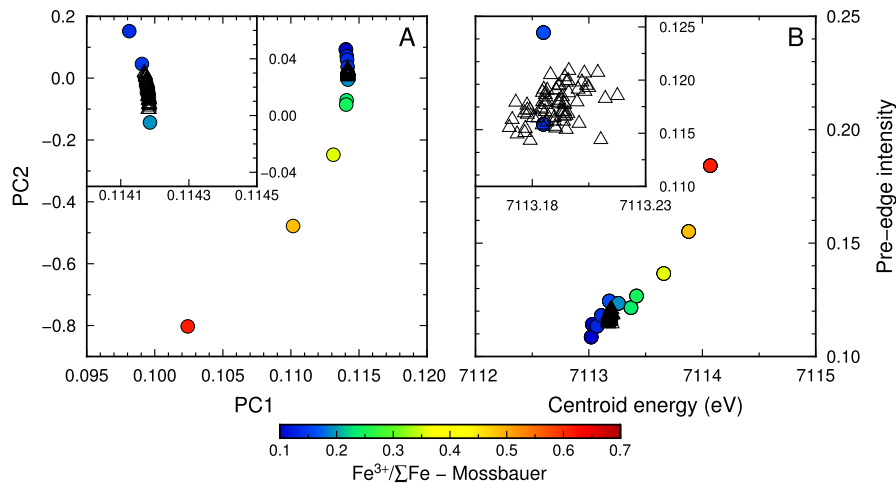


**Fig. 4.** Assessment of spectral similarity between the samples and standards. (A) The PC1 and PC2 scores from sample spectra are plotted as open triangles and reference spectra from reference block NMNH 117393 as circles coloured by their  $\text{Fe}^{3+}/\Sigma\text{Fe}$  (Cottrell and Kelley, 2009). Inset shows a magnification of the region occupied by the samples. (B) Centroid energies and pre-edge intensities calculated for the same reference and sample spectra. Samples and standards overlap in PC1–PC2 and centroid energy–pre-edge intensity, indicating the validity of 1) projecting the principal component scores of the samples to  $\text{Fe}^{3+}/\Sigma\text{Fe}$  using linear mixing of the known standard glasses, and 2) using the standards to calibrate the unknowns.

different calibrations is  $\sim 0.1\%$ , more than an order of magnitude less than the systematic change we observe along-ridge towards Iceland. Repeat analyses of an in-house reference glass over the same period gave a  $1\sigma$  reproducibility of 0.16%, which is the precision we quote in subsequent figures.

To estimate the uncertainty in the calibration that derives from the linear model fit to the Mössbauer data and the precision of the Mössbauer data itself, we have performed Monte Carlo modelling. The modelling starts with the raw spectra, randomly adds noise to the spectra assuming Poisson counting statistics on each point, re-performs PCR permuting each Mössbauer measurement of  $\text{Fe}^{3+}/\Sigma\text{Fe}$  on the NMNH 117393 glasses by the uncertainty quoted in Cottrell and Kelley (2009), and then calculates a new set of calibration parameters. There is a high degree of correlation between the intercept ( $a_0$ ) and coefficient for PC1 ( $a_1$ ), indicating a trade-off in their influence on  $\text{Fe}^{3+}/\Sigma\text{Fe}$ . In contrast, the coefficient for PC2 ( $a_2$ ) is largely independent of the value chosen for  $a_0$  or  $a_1$ , as expected given the orthogonal basis provided by PCA.

Propagating the error matrix for the PCR calibration parameters through to  $\text{Fe}^{3+}/\Sigma\text{Fe}$  using the general formula

$$\sigma^2 = \mathbf{p}\Sigma^a\mathbf{p}^T, \quad (3)$$

gives an external  $1\sigma$  precision of 0.4% (where  $\mathbf{p}$  is the vector of principal component scores and  $\Sigma^a$  is the covariance matrix for the model parameters, see Table A.2 for values). This precision is still less than half of the total along-ridge shift in  $\text{Fe}^{3+}/\Sigma\text{Fe}$  we observe. However, for the remainder of this paper we use the external reproducibility of 0.16% as our error term on the data, since we are focusing on the relative difference between samples rather than systematic shifts that could result from error in the calibration.

### 3. Results

The 700 km transect of mantle represented by the Reykjanes Ridge samples incorporates both the long-wavelength transition from background MORB-like compositions in the south to strongly mantle plume-influenced in the north, and short-lengthscale heterogeneities in the form of seamounts (Murton et al., 2002). The raw  $\text{Fe}^{3+}/\Sigma\text{Fe}$  from these samples is presented in Fig. 5A as a function of radial distance from the Iceland plume centre (Shorttle and MacLennan, 2011). At any given distance, more

evolved basalts with lower MgO are more oxidised than primitive basalts, confirming the importance of low pressure fractionation in modifying primary  $\text{Fe}^{3+}/\Sigma\text{Fe}$  (Bézos and Humler, 2005; Cottrell and Kelley, 2011). Nevertheless, long-wavelength structure is apparent, with basalts at a similar MgO showing a progressive shift to higher  $\text{Fe}^{3+}/\Sigma\text{Fe}$  closer to Iceland. The seamount 14D (labelled square symbols Fig. 5A) has also captured short-lengthscale heterogeneity, which, given its MgO, is as oxidised as basalts 700 km closer to Iceland.

#### 3.1. Accounting for crystal fractionation

The sensitivity of  $\text{Fe}^{3+}/\Sigma\text{Fe}$  to low pressure fractionation has been previously demonstrated in MORB suites analysed by XANES (Cottrell and Kelley, 2011). Four lines of evidence indicate that fractionation has also affected the Reykjanes Ridge suite of basalts studied here:

1. MgO concentrations of the Reykjanes Ridge glasses fall between 6.5 and 9 wt% MgO. Given that a primary MORB will have  $\sim 10$  wt% MgO, significant fractionation of at least olivine must have occurred in all these samples.
2. There is abundant petrological evidence from these samples of olivine macrocrysts, and in many cases plagioclase and clinopyroxene crystals (Murton, 1995).
3. Major element trends of Al and Ca with Mg (Fig. A.2), and trace element trends of Eu also indicate plagioclase and clinopyroxene fractionation (Murton et al., 2002).
4. It is clear from Figs. 5 and 6 that crystal fractionation has also played an important role in determining  $\text{Fe}^{3+}/\Sigma\text{Fe}$  in Reykjanes Ridge magmas.  $\text{Fe}^{3+}/\Sigma\text{Fe}$  is systematically higher at a given distance from the plume centre in the most evolved samples (those with lowest MgO) compared with more primitive basalts.

Crystal fractionation is therefore likely to be generating scatter in the along-ridge trend that is not associated with mantle source or processes. However, despite the need to correct  $\text{Fe}^{3+}/\Sigma\text{Fe}$  for fractionation, we emphasise that the existence of long- and short-lengthscale variability in  $\text{Fe}^{3+}/\Sigma\text{Fe}$  around Iceland is not predicated upon applying this correction to the data.

For the fractionation correction we tested both Petrolog (Danyushevsky and Plechov, 2011) reverse fractionation calcu-

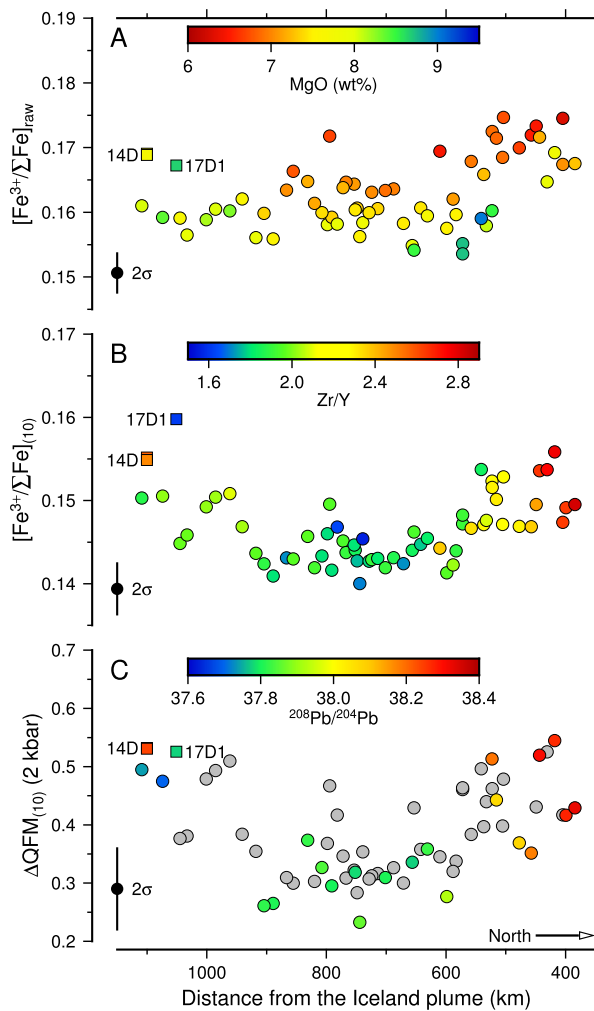


**Fig. 5.** The along-ridge increase in  $\text{Fe}^{3+}/\Sigma\text{Fe}$  and oxidation approaching Iceland. (A) Raw  $\text{Fe}^{3+}/\Sigma\text{Fe}$  is plotted as a function of radial distance from the Iceland plume centre, and coloured by the MgO content of the sample glasses. Labelled square symbols are the samples identified as exhibiting geographically anomalous geochemical signals, of which the two 14D samples are enriched basalts from a seamount (Murton et al., 2002). (B)  $\text{Fe}^{3+}/\Sigma\text{Fe}$  after correction for low pressure fractionation to 10 wt% MgO, with points coloured by Zr/Y. (C) Samples have been projected to their  $\log(f\text{O}_2)$  relative to the QFM buffer at 2 kbar using the equation of Kress and Carmichael (1991); points are coloured by their Pb isotopic composition. In each panel the transition to more oxidised compositions occurs at  $\sim 600$  km, concurrent with increases in indices of mantle enrichment such as Zr/Y and  $^{208}\text{Pb}/^{204}\text{Pb}$ . Trace element and isotope data from Murton et al. (2002), Thirlwall et al. (2004).

lations, and two-stage empirical and olivine addition models (Figs. A.3 and A.2). Both methods gave very similar results and we chose the empirical method for its simplicity.

To apply any fractionation correction, an estimate is required of the MgO at which olivine-only crystallisation transitions to olivine + clinopyroxene + plagioclase crystallisation. We identified this point using an optimisation algorithm to find the MgO split that produces the two high- and low-MgO vs. major element regressions with minimum misfit. The MgO found with this method was 8.0 wt%. Samples below 8.0 wt% MgO had their major element compositions shifted parallel to a York (1969)-style fit to the low MgO data, until at 8 wt% MgO (Fig. 6). Further correction to 10 wt% MgO, or until the liquid was in equilibrium with  $\text{Fo}_{90}$ , was performed with simple olivine addition using the Herzberg and O'Hara (2002) model. The key result of applying this fractionation correction to the data is that it does not remove the sense of along-ridge shift to more oxidised compositions (Fig. 6).

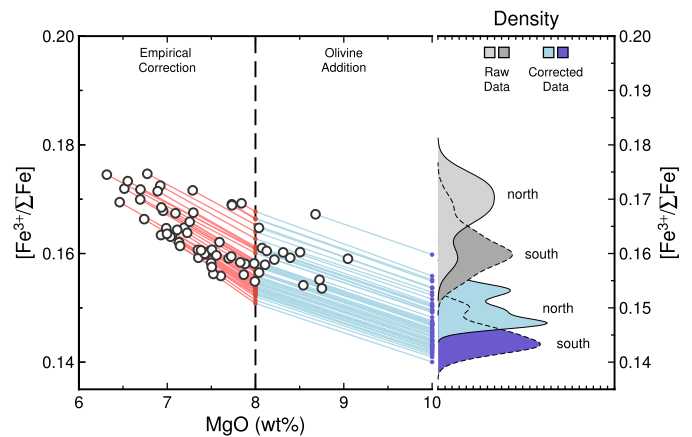


**Fig. 6.** The path of reverse fractional crystallisation applied to the Reykjanes Ridge samples. The starting chemistry of each sample is marked by an open circle and the lines extending to higher MgO mark the reverse fractional crystallisation path. Samples with less than 8 wt% MgO were first corrected back to 8 wt% MgO by best-fit regression to their major element data. This empirical correction accounts for liquid fractionation in the olivine + plagioclase + clinopyroxene (i.e. gabbro) field. Subsequent reverse fractionation from 8 wt% MgO to 10 wt% MgO is performed by olivine addition using the Herzberg and O'Hara (2002) model. The side panel presents kernel density estimates of the dataset split into samples from the northern sector of the Reykjanes Ridge ( $> 61.5^\circ\text{N}$  and within 480 km of the plume centre, solid lines with light grey or light blue fill) and samples from the southern sector ( $\leq 61.5^\circ\text{N}$  and further than 480 km from the plume centre, dashed lines with dark grey or dark blue fill). Filled grey kernel density estimates are for the raw dataset (open circles), whilst blue filled kernel density estimates are for the data with the fractionation correction applied. For both the raw and corrected data basalts from the southern sector of the ridge are less oxidised than those from the northern sector.

### 3.2. The effect of degassing

From a mantle geochemical perspective, it is important to exclude the null hypothesis that the along-ridge trends in  $\text{Fe}^{3+}/\Sigma\text{Fe}$  are a result of systematic along-ridge degassing. As the Reykjanes Ridge shallows, samples are erupted under progressively lower confining pressures, allowing for more syn-eruptive degassing prior to quenching. To account for the long-wavelength trend of increasing oxidation towards Iceland (Fig. 5B), degassing would need to: (1) involve a net transfer of electrons from the melt to the gas phase; and (2) involve the redox-influencing gas phase(s) beginning significant degassing over the depth interval where we observe an increase in basalt  $f\text{O}_2$ . Whether either of these conditions apply can be tested both empirically and with degassing models.

The long-wavelength trend of increasing oxidation towards Iceland is broken by the three most northerly samples (Fig. 5B). These basalts were erupted in the shallowest water ( $< 500$  m) of the sample suite, and have  $\text{Fe}^{3+}/\Sigma\text{Fe} \sim 0.05$  lower than the samples immediately to their south. The low pressure of eruption makes these samples the most likely to have experienced degassing. Degassing of the most northerly samples is consistent with their lower S content compared with other samples (Fig. 7A, triangle symbols) and with their  $\text{H}_2\text{O}$  contents (Nichols et al., 2002), which are slightly lower than the trend of increasing  $\text{H}_2\text{O}$  towards Iceland would predict. Given the evidence for degassing, the offset of these samples to lower  $\text{Fe}^{3+}/\Sigma\text{Fe}$  suggests that degassing has reduced them. If this is the case, then the longer wavelength trend of increasing oxidation towards Iceland is unlikely to be due to degassing, and therefore degassing as a null hypothesis cannot explain a majority of the data.

We can also assess the influence of degassing on Reykjanes Ridge basalts with degassing models. As discussed above, the basalts erupted in water depths of  $< 500$  m will have been the most strongly affected by  $\text{H}_2\text{O}$  and S loss, while  $\text{CO}_2$  degassing will have been significant for all samples (Dixon et al., 1991). Of these volatile species, sulfur has the greatest potential leverage on magma redox state; this has been shown both theoretically

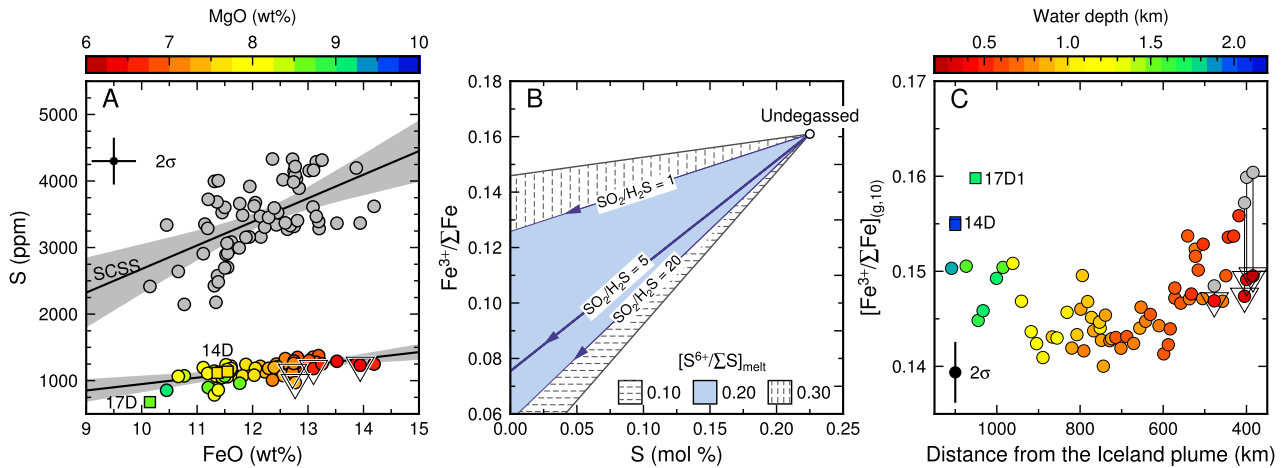
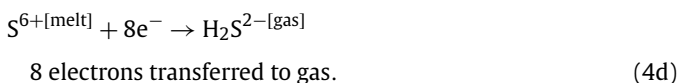
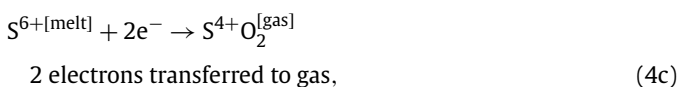


**Fig. 7.** A quantification of how S degassing may have affected the redox state of Reykjanes Ridge basalts. (A) The sulfur content of samples plotted against their iron content (symbols coloured by MgO), with a regression and 95% confidence envelope. Samples erupted in less than 500 m water depth have a triangle plotted over them. The correlation between S and FeO implies that basalts may be sulfide saturated. However, calculating the predicted sulfur content at sulfide saturation (Liu et al., 2007) assuming  $T = 1100^\circ\text{C}$  and  $P = 1000$  bar (grey symbols) implies that the samples are undersaturated in sulfur. (B) A simple model investigating the effects of Eqs. (4a)–(4d) on the oxidation state of the liquid during sulfur degassing. Degassing calculations are performed with the  $\text{S}^{6+}$  fraction in the liquid as 10% (horizontal dashed region), 20% (blue region, our preferred value) and 30% (vertical dashed region) which then degasses as an  $\text{SO}_2$ – $\text{H}_2\text{S}$  mix (we calculate degassing trajectories for  $\text{SO}_2/\text{H}_2\text{S}$  ratios between 1 and 20). Our preferred estimate of  $\text{SO}_2/\text{H}_2\text{S}$  in the gas, consistent with the measured  $f_{\text{O}_2}$  of Reykjanes Ridge basalts, is 5. In all cases investigated degassing reduces the basalts, lowering  $\text{Fe}^{3+}/\Sigma\text{Fe}$ . (C) Degassing and fractionation-corrected ferric iron proportions ( $[\text{Fe}^{3+}/\Sigma\text{Fe}]_{(g,10)}$ ) after applying the full Gaillard et al. (2011) degassing model to the samples erupted in less than 500 m water depth, plotted as a function of distance from the Iceland plume. For these samples the original ferric iron proportions (coloured symbols) have been recalculated back to a water depth of 500 m (grey symbols joined to coloured symbols), largely removing the effect of S degassing. (For interpretation of the references to colour in this figure legend, the reader is referred to the web version of this article.)

(Burgisser and Scaillet, 2007) and in nature (Moussallam et al., 2014). Writing in terms of half reactions, sulfur degassing could proceed by



If we make the additional assumption that Fe, as the dominant heterovalent species in a melt, accommodates all the electron exchange, then these reactions are capable of producing large shifts in Fe oxidation state. The direction of redox change depends on the initial sulfur speciation in the liquid and the sulfur species formed in the gas phase, with sulfur degassing being capable of both reduction (Eq. (4a)) and oxidation of magma (Eqs. (4c) and (4d)).

In nature, multiple sulfur degassing pathways will be exploited (e.g. Gaillard et al., 2011); their relative importance as a function of melt composition and pressure will determine the net redox effect on the melt. A key parameter in determining the mode of sulfur degassing will be its speciation in the melt (Eqs. (4a)–(4d)). For Reykjanes Ridge basalts with their measured  $\Delta\text{QFM}$  from +0.3 to +0.6,  $\text{S}^{2-}$  will be the dominant sulfur species in the liquid (Jugo, 2009) (at this  $f_{\text{O}_2}$  a maximum of 10% of the S is in the  $\text{S}^{6+}$  state). Sulfur loss from these basalts as  $\text{SO}_2$  will therefore reduce them (Eq. (4a)), whereas sulfur loss as  $\text{H}_2\text{S}$  is redox neutral (Eq. (4b)). The precise proportions of  $\text{SO}_2$  and  $\text{H}_2\text{S}$  being lost from the melt will depend on the pressure and temperature of degassing, but the key point is that, provided S in the melt is dominantly  $\text{S}^{2-}$ , this degassing will be reducing. Fig. 7B shows a simple model implementing the redox stoichiometries outlined in Eqs. (4a)–(4d). Even

in an unrealistically oxidising case where 30% of the sulfur in the melt is present as  $\text{S}^{6+}$  and degasses to 1:1  $\text{H}_2\text{S}:\text{SO}_2$ , the basalts are reduced by degassing.

The results from our simple calculations (Fig. 7B) are confirmed when we correct for degassing with the full thermodynamic model of Gaillard et al. (2011), which predicts sulfur solubility and speciation in the liquid and gas phases. For these calculations we take the  $\text{H}_2\text{O}$  data from Nichols et al. (2002) and our measured  $f_{\text{O}_2}$ . There are two important results from our application of the Gaillard et al. (2011) model: Firstly, it predicts significant sulfur loss only for basalts erupted in < 500 m water depth; therefore, most samples experienced insufficient S degassing to explain the oxidation trend observed for basalts erupted in 1000 m of water (Fig. 7C). Secondly, the Gaillard et al. (2011) model predicts that, at the oxidation state of the Reykjanes Ridge basalts ( $\Delta\text{QFM} \sim +0.5$ ), the molar ratio of degassing  $\text{SO}_2/\text{H}_2\text{S}$  is > 5 over all pressures considered (equivalent water depths from 300 m to > 1000 m). As a result, applying the model to correct  $\text{Fe}^{3+}/\Sigma\text{Fe}$  in the four most degassed samples back to their pre-degassing (500 m water depth) values restores these samples to the long-wavelength trend of increasing oxidation towards Iceland (Fig. 7C).

In summary, neither the onset of significant S degassing (at  $\sim 500$  m water depth) nor its redox effect (reducing) are consistent with the observed trend of basalts becoming more oxidised towards Iceland.

### 3.3. The fractionation corrected dataset

In the remainder of this paper we use the Reykjanes Ridge data corrected for fractional crystallisation, but uncorrected for degassing: we prefer to use the minimally corrected dataset that still shows significant structure and, as shown above, degassing will only have diminished the trend of along-ridge oxidation.

In the fractionation-corrected dataset the along-ridge transition to more oxidised samples closer to Iceland remains. However, the samples furthest from Iceland (> 1000 km) also appear to show a slight increase in  $\text{Fe}^{3+}/\Sigma\text{Fe}_{(10)}$  compared with those at intermediate distances, creating a U-shaped along-ridge profile. This is true even excluding samples 17D1 and 14D.

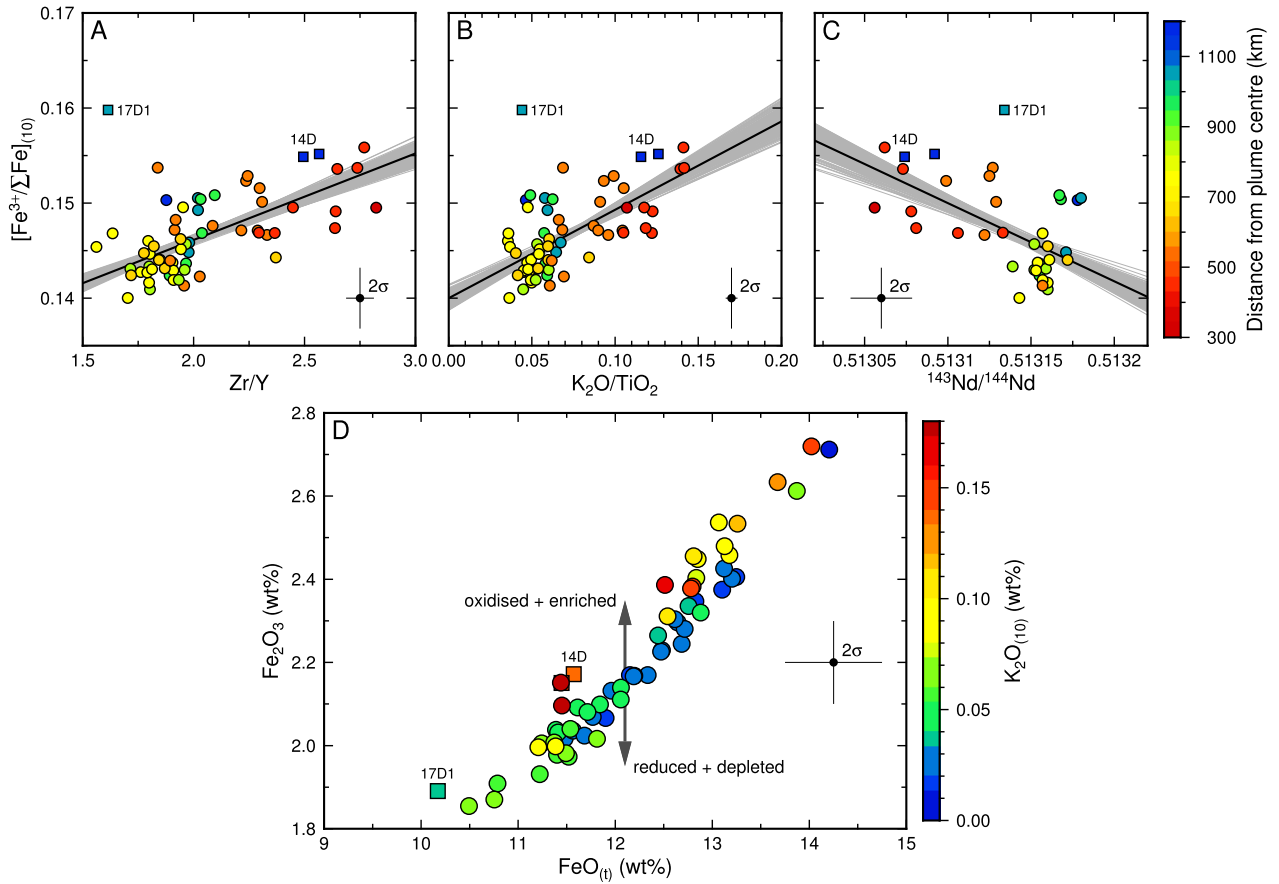


**Fig. 8.** Correlation between oxidation and geochemical indices of enrichment, Zr/Y (A),  $K_2O/TiO_2$  (B),  $^{143}Nd/^{144}Nd$  (C). Black lines represent weighted regressions through the data (York, 1969), and grey lines simulations where the data has been randomly permuted according to its analytical uncertainty, indicating the stability of the regression result. Correlations between  $[Fe^{3+}/\Sigma Fe]_{(10)}$  and tracers of incompatible element enrichment are significant at the 95% level. In (D) the relatively greater oxidation of the most enriched samples is shown in  $Fe_2O_3-FeO_t$  space, colouring the symbols by their fractionation corrected potassium content ( $K_2O_{(10)}$ ). At a given  $FeO_t$ , samples with higher  $K_2O_{(10)}$  tend to have a higher  $Fe_2O_3$ . 17D1 is excluded from this analysis because of its non-Iceland plume affinity (Murton et al., 2002). Trace element and isotope data from Murton et al. (2002), Thirlwall et al. (2004), Hilton et al. (2000).

The range of  $Fe^{3+}/\Sigma Fe_{(10)}$  in the dataset,  $\sim 0.015$ , is equivalent to the range in global primitive MORB (Cottrell and Kelley, 2013) (Fig. 5B). This similarity in absolute variability found in Cottrell and Kelley (2013) and our regional dataset is also present when  $Fe^{3+}/\Sigma Fe_{(10)}$  is used to calculate the basalts' oxygen fugacity as  $\log(fO_2)$  with respect to QFM buffer,  $\Delta QFM_{(10)}$  (Fig. 5C, Kress and Carmichael, 1991). Samples close to Iceland vary in  $fO_2$  by  $\sim 0.25 \log(fO_2)$  units, compared to  $\sim 0.3 \log(fO_2)$  units in global primitive MORB (Cottrell and Kelley, 2013). Although the amplitudes of redox shifts are similar, the major difference between the global MORB dataset (Cottrell and Kelley, 2013) and our dataset is that we find both trace element and isotopic enrichment to be consistently associated with oxidation. This relationship holds over the 100 km scale, where increases in incompatible trace element ratios (e.g. Zr/Y) and isotope ratios (e.g.  $^{208}Pb/^{204}Pb$ ) match increasing  $Fe^{3+}/\Sigma Fe_{(10)}$  (Fig. 5B and C); and is present on the 10 km scale of the enriched basalts sampled from seamount 14D.

Fractionation-corrected  $Fe^{3+}/\Sigma Fe_{(10)}$  shows statistically significant correlations with the incompatible element enrichment recorded by trace element ratios and isotope systems (Fig. 8). Sample 17D1 was not included in the regression analysis of Fig. 8 because of its unique composition (Murton et al., 2002): despite relatively low La/Yb, Zr/Y,  $K_2O/TiO_2$  and absolute incompatible element concentrations, 17D1 has high  $^3He/^4He$  and is moderately oxidised. Whilst 17D1 may represent a distinct component within the plume mantle (Thirlwall et al., 2004), its geochemical char-

acteristics are not reflected in the rest of the data so we do not consider this sample any further.

## 4. Discussion

### 4.1. The control of melting processes on basalt $fO_2$

Given the observed along-ridge oxidation towards Iceland (Fig. 5) and the correlation of this oxidation with lithophile element and radiogenic isotope tracers of enrichment (Fig. 8), the key question is what source or process relates enrichment to increased oxidation. One challenge we face is that the correlation between source and mantle potential temperature inherent to our dataset makes it difficult to identify causal relationships between enrichment, melting style and  $fO_2$ . This problem is likely to apply in general to plume-scale transects of basalt chemistry. However, by considering both the long- and short-lengthscale chemical structure along the Reykjanes Ridge we can begin to separate the roles of source and temperature.

The mantle potential temperature increases towards Iceland by  $> 130^\circ C$  (White et al., 1995; Shorttle et al., 2014), implying an associated increase in the mean pressure and extent of melting, and a higher pressure of initial solidus intersection. Higher mean extents of melting should cause  $Fe^{3+}/\Sigma Fe_{(10)}$  to decrease towards Iceland, because  $Fe_2O_3$  behaves moderately incompatibly during mantle melting (Canil et al., 1994). This process may in fact be controlling the slight northwards decrease in  $Fe^{3+}/\Sigma Fe_{(10)}$  observed in the most distant samples (Fig. 5B): a region where the plume's thermal influence is present and increasing northwards,



but the chemical signature may be weak (Shorttle et al., 2010; Jones et al., 2014). That increasing  $\text{Fe}^{3+}/\sum\text{Fe}_{(10)}$  is also observed in the basalts erupted closest to Iceland indicates that some other process or source factor must come to dominate over the dilution of  $\text{Fe}_2\text{O}_3$  by melting degree. This is also clear from the ratios (Figs. 5 and 8) and raw concentrations (Murton et al., 2002) of incompatible elements, which increase towards Iceland despite progressively higher extents of melting.

It is hard to reconcile the geochemistry of seamount 14D, which is oxidised and enriched, with changes in the temperature and pressure of melting as being the primary drivers of  $f\text{O}_2$  variability along-ridge. On the lengthscale of seamount 14D, which is within 30 km of otherwise more reduced and depleted basalts on the southern Reykjanes Ridge, background temperature changes are likely to be minimal. As many of the geochemical characteristics of 14D are also the same as strongly plume-influenced basalts erupted closer to Iceland (Hilton et al., 2000; Murton et al., 2002; Thirlwall et al., 2004) it is likely that both the long- and short-lengthscale structures in  $f\text{O}_2$  are explained by the same phenomenon. Only changes in source composition are likely to be present at high amplitude on both long and short lengthscales down the Reykjanes Ridge, and be capable of modifying both the oxidation state and isotope chemistry of basalts. 14D does not coincide with a V-shaped ridge crest or trough (Jones et al., 2014).

Mantle potential temperature will also have an effect on ferric iron through its influence on the mineral and volatile assemblages buffering melting. If the source is graphite-buffered then higher pressures of initial melting towards Iceland could produce more oxidised basalts, as graphite leaves the residue earlier along the decompression path (Ballhaus and Frost, 1994). Taking the increase in the initial pressure of melting towards Iceland to be  $\sim 1$  GPa (Shorttle et al., 2014), the earlier loss of graphite buffering under northern ridge segments could oxidise basalts by  $\sim 0.4 \log(f\text{O}_2)$  units relative to those further south. However, both MORB and Reykjanes Ridge samples are too oxidised to be in equilibrium with a graphite-bearing source (Cottrell and Kelley, 2011). So a varying pressure of graphite exhaustion cannot be driving the observed changes in  $\text{Fe}^{3+}/\sum\text{Fe}$  or  $\Delta\text{QFM}_{(10)}$  between samples.

A separate role for mantle carbon influencing the oxidation state of erupted basalts has been proposed by Cottrell and Kelley (2013) and Stagno et al. (2013), who considered how variations in the absolute amount of carbon between mantle domains may affect  $f\text{O}_2$ . In this model the redox melting of carbon to carbonate during decompression reduces the ferric iron in silicates leaving a more reduced source. If the carbon content of enriched mantle is higher than that of ambient MORB mantle then enriched domains will produce more reduced silicate melts as more of their ferric iron is reduced during redox melting of carbon (Cottrell and Kelley, 2013). However, towards Iceland both the incompatible trace element content and  $\text{Fe}^{3+}/\sum\text{Fe}_{(10)}$  of basalts increase. For example, the higher Nb content of near-Iceland basalts (Murton et al., 2002) could imply a mantle source 10-fold enriched in carbon with respect to MORB (Saal et al., 2002). If this carbon underwent redox melting then we would expect the enriched basalts near Iceland (and the seamount 14D) to be the most reduced, the opposite to what is observed. Therefore, accounting for redox melting would imply a very oxidised enriched Icelandic source, so that following carbon oxidation the silicate residue could still produce melts oxidised relative to MORB.

Ultimately, understanding the effect of simple changes in melt region parameters on the oxidation state of aggregate basalts will require more comprehensive thermodynamic models of mantle melting. These models face a significant challenge in needing to incorporate carbon–sulfur–silicate buffering in addition to silicate phase changes and pressure-dependent solid solutions. However, with our current understanding of melt region redox processes it

appears likely that an intrinsically oxidised component is required in the Icelandic mantle to explain the relationships seen in Figs. 5 and 8.

#### 4.2. The origin of an enriched and oxidised Icelandic source component

To relate our observations to solid Earth oxygen fluxes, an important question is how the enriched Icelandic source became oxidised. One possibility is that this occurred by metasomatic enrichment, either through carbonatitic fluids as has been suggested for lithospheric peridotites (Canil et al., 1994), via hydrous metasomatism as may occur at subduction zones (Kelley and Cottrell, 2009), or by addition of small fraction silicate melts. Whilst it is difficult to place unique constraints on the origin of enriched sources, especially as the process may have been polyphase, we can assess each metasomatic mechanism for consistency with other major and trace element data.

Canil et al. (1994) found that carbonatitic metasomatism, in addition to raising  $f\text{O}_2$ , raised  $\text{CaO}/\text{Al}_2\text{O}_3$  in peridotites. However, this major element signal of carbonatite interaction is the opposite of what we see in enriched Icelandic basalts (Shorttle and Maclennan, 2011).

The second possibility is that the Icelandic source was enriched in a subduction zone setting, transferring both fluid-mobile trace elements and high  $f\text{O}_2$ , as is inferred to be happening beneath modern arcs (Kelley and Cottrell, 2009). To address this we have calculated the apparent relative compatibility of  $\text{Fe}_2\text{O}_3$  and trace elements in our sample suite (Fig. 9A, Sims and DePaolo, 1997; Hémond et al., 2006; Stracke et al., 2003a). In the case of metasomatic hydrous enrichment we would expect: 1. fluid-mobile elements such as Sr, Pb, U, Cs, Rb and Ba to be relatively enriched compared with less fluid-mobile trace elements of similar solid-melt partitioning (as indicated by high gradients in  $\log(\text{element})$  vs.  $\log(\text{Fe}_2\text{O}_3)$  space); 2. for  $\text{Fe}_2\text{O}_3$  to show the strongest correlation with these fluid-mobile elements; and 3. apparent  $\text{Fe}_2\text{O}_3$  partition coefficients much less than the bulk  $D_{\text{Fe}_2\text{O}_3} = 0.1$  predicted for peridotite (O'Neill et al., 1993; Canil et al., 1994). However, Fig. 9A shows that the apparent partition coefficient for  $\text{Fe}_2\text{O}_3$  is most similar to that of Gd ( $\sim 0.1$ ), consistent with predicted solid-melt equilibria. The correlations between  $\text{Fe}_2\text{O}_3$  and fluid-mobile elements, although high, are also weaker than for similarly incompatible non-fluid-mobile elements. Despite being enriched, the fluid-mobile elements are less enriched than would be expected given their very low partition coefficients during peridotite melting.

A third mechanism for transferring ferric iron to the Icelandic source is by adding small fraction melts of a typical lherzolitic source ( $\text{Fe}_2\text{O}_3 = 0.3$  wt%). For  $D_{\text{Fe}_2\text{O}_3} = 0.1$ , adding  $< 5\%$  of metasomatic melt by mass to a lherzolite can generate a source with sufficiently high  $\text{Fe}_2\text{O}_3$  to explain its observed increase along ridge. However, the mass balance of this metasomatism would again fail to match the observed major element characteristics of the enriched Icelandic source component, which requires a 50:50 lherzolite:basalt mixture (Shorttle and Maclennan, 2011).

Following the reasoning above we reject the possibility that oxidised hydrous/carbonatitic fluids or small fraction melts were important in generating the enriched Icelandic source characteristics. Instead, given the evidence for pyroxenitic components in the Iceland plume source (Chauvel and Hémond, 2000; Stracke et al., 2003b; Shorttle and Maclennan, 2011; Sims et al., 2013), we instead consider that the enriched oxidised component is ancient recycled seafloor. Oceanic crust will be enriched in  $\text{Fe}_2\text{O}_3$  relative to ambient mantle simply by ferric iron's incompatibility during partial melting, but significant secondary enrichment may also occur during hydrothermal alteration through sulfate reduction at the ridge axis (Lécuyer and Ricard, 1999; Sleep, 2005). De-watering

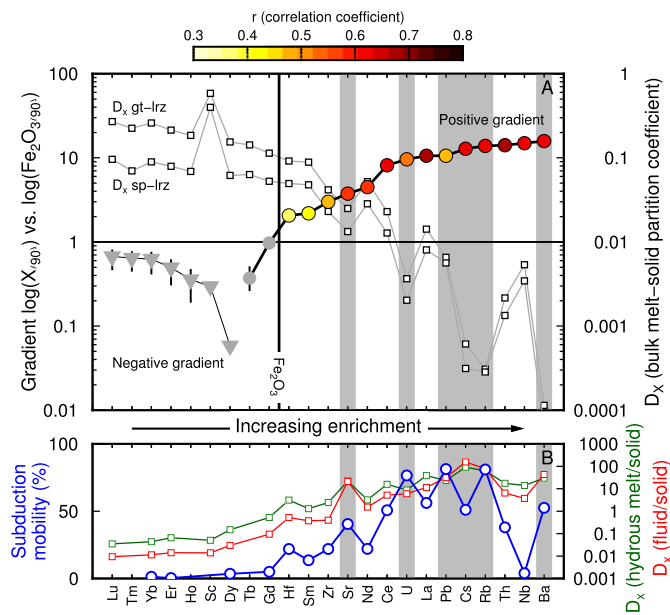


**Fig. 9.** The apparent relative compatibility of trace elements in our sample set relative to  $Fe_2O_3$  (Sims and DePaolo, 1997; Hémond et al., 2006). (A) Trace element data corrected for fractional crystallisation to  $Fo_{90}$  have been plotted against  $Fe_2O_3$  in a log–log plot and the gradient and correlation coefficient calculated. Circles record positive gradients and triangles negative gradients (absolute values plotted); coloured symbols have correlations significant at  $> 95\%$  confidence level, and error bars are 95% confidence bounds on the calculated gradients. A gradient of unity in  $\log(\text{trace element})$  vs.  $\log(Fe_2O_3)$  space indicates similar compatibility between the two elements considered, placing the effective compatibility of  $Fe_2O_3$  close to Gd. Square symbols record the bulk garnet lherzolite– and spinel lherzolite–melt partition coefficients (Gibson and Geist, 2010), implying  $D_{Fe_2O_3} \sim 0.1$ . Elements exhibiting under-enrichment with respect to their silicate–melt partition coefficients are highlighted in grey. (B) The mobility of trace elements during subduction from Stracke et al. (2003a) (circles) and the experimentally determined hydrous melt–solid and fluid–solid partition coefficients of Kessel et al. (2005). Trace elements exhibiting relative under-enrichment compared to that predicted by their silicate–melt partition coefficients systematically exhibit higher fluid-mobility during subduction zone processing.

of the slab during subduction could then account for the relative under-enrichment of fluid-mobile trace elements in the enriched Icelandic source (Fig. 9B).

#### 4.3. Estimating the ferric iron content of enriched Icelandic mantle

None of the melt compositions in the Reykjanes Ridge suite are representative pure melts of single mantle domains. Instead they will be mixtures of melts from the enriched pyroxenitic and depleted lherzolitic Icelandic source components (Shorttle and MacLennan, 2011; Shorttle et al., 2014). Therefore, to constrain the origin of the enriched oxidised component we first need to estimate its  $Fe_2O_3$ , which will be more extreme than is recorded in any basalts we have sampled.

To determine  $Fe_2O_3$  in primitive melts from the enriched source we have regressed  $Fe_2O_3(Fo_{90})$  (ferric iron corrected to be in equilibrium with  $Fo_{90}$  olivine) from our samples against an estimate of the proportion of pyroxenite-derived melt contributing to their bulk chemistry (Fig. 10). The calculations to determine the pyroxenite-derived melt fraction in Icelandic plume basalts have been discussed in detail by Shorttle et al. (2014); the basic reasoning is that the chemical diversity of sampled basalts from onland Iceland makes it possible to identify the enriched and depleted endmember melt compositions being supplied from the mantle. These endmember melt compositions can then be used to form a mass balance to produce the incompatible trace element chemistry of derivative mixed melts, thus constraining the proportion of each endmember melt in the mixture. The intersection of the regression in Fig. 10A with the  $Fe_2O_3(Fo_{90})$  axis at 100% pyroxenite-

derived melt constrains the  $Fe_2O_3(Fo_{90})$  in primary melts of the enriched Icelandic source to be  $\sim 1.8$  wt%–2.0 wt%. Depleted melt compositions are assumed to be represented by the most depleted basalts along the Reykjanes Ridge (at 0% pyroxenite-derived melt) with  $Fe_2O_3(Fo_{90}) \sim 1.5$  wt%.

We next need to project this melt composition into an estimate of ferric iron in the source ( $[Fe_2O_3]_{\text{source}}$ ). For this we use the aggregate fractional melting equation  $C_l = C_0(1/F(1 - (1 - F)^{1/D_{Fe_2O_3}}))$ , where  $C_l$  is the liquid composition,  $C_0$  the solid composition,  $F$  the melt fraction, and  $D_{Fe_2O_3}$  the bulk ferric iron partition coefficient. We calculate bulk partition coefficients from the mineral–melt partition coefficients given in Mallmann and O'Neill (2009) and considering garnet–melt partition coefficients between 0.85 and 1. We take a source mineralogy for the depleted Icelandic source component of a spinel lherzolite (Shorttle and MacLennan, 2011),  $sp_{27}:ol_{55}:opx_{25}:cpx_{18}$  (spinel:olivine:orthopyroxene:clinopyroxene). Two mineral modes are tested for the pyroxenitic lithology (Shorttle and MacLennan, 2011; Kogiso et al., 1998): a garnet-bearing source  $gt_{27}:ol_{23}:cpx_{50}$  (gt = garnet) and a spinel-bearing source  $sp_{7}:ol_{18}:opx_{15}:cpx_{60}$ . These source mineralogies and partition coefficients are then combined to produce the range of bulk  $D_s$  in Table A.3, of which the extremes are used in calculating the bounds on our estimates of source  $Fe_2O_3$ . Melt fractions used in the calculations are taken from the model results of Shorttle et al. (2014), as reasonable estimates of mean degree of melting of peridotite and pyroxenitic lithologies given the requirement to match along-ridge crustal thicknesses (Smallwood and White, 1998; Navin and Sinha, 1998). The combination of melt fractions and partition coefficients used to produce the preferred and upper and lower bounds for each lithology in Fig. 10 are given in Table A.4.

Fig. 10B shows that whilst the depleted basalts in our dataset are well matched by melting of a typical upper mantle peridotite with  $Fe_2O_3 = 0.3$  wt%, the enriched source must contain between 0.9 and 1.4 wt%  $Fe_2O_3$ . This  $Fe_2O_3$  range falls between sources containing regular MORB and (oxidised) altered oceanic crust (Fig. 10C). Although our calculations cannot uniquely identify the source composition, they illustrate the key parameters that need to be constrained to arrive at a source estimate.

#### 4.4. Implications for oxygen cycling

The results above leave open the possibility of the solid Earth having an important role in oxygen cycling through the subduction of altered oxidised oceanic crust which is eventually remelted at plume settings such as Iceland. Oxidation of the seafloor during hydrothermal circulation has only been efficient since global surface oxygenation generated appreciable sulfate concentrations in the oceans (Sleep, 2005; Kasting, 2013). Some estimates of the age of the enriched component in the Icelandic source place it at  $\sim 400$  Ma (McKenzie et al., 2004; Thirlwall et al., 2004), consistent with the requirement for oxic conditions to have been present in the deep ocean at the time of the source's formation (Canfield et al., 2007). The present-day eruption of oxidised basalts from the Iceland plume may therefore represent closure of the global oxygen cycle as envisaged by Lécuyer and Ricard (1999), as oxygen sequestered into the solid Earth by subduction is returned to the surface environment.

## 5. Conclusions

A suite of 64 Reykjanes Ridge basalts sampling long- and short-wavelength chemical and isotopic structure in the Iceland plume record changes in oxidation that correlate with enrichment: enriched basalts from closest to the Iceland plume and from a seamount with a plume geochemical affinity, have higher  $Fe^{3+}/\sum Fe$  by up to 0.015 and higher  $\Delta QFM$  by 0.25  $\log(fO_2)$

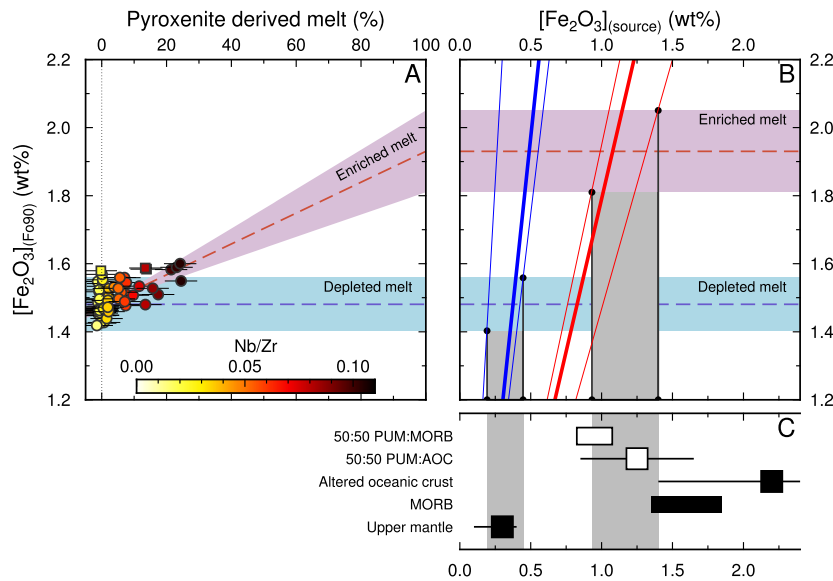


**Fig. 10.** Determining the  $\text{Fe}_2\text{O}_3$  concentration of the enriched Icelandic plume component. (A) The proportion of recycled pyroxenite melt contributing to basalt compositions is estimated using the method of Shorttle et al. (2014). This estimate is regressed (dashed line with 95% confidence interval) against the fractionation-corrected  $[\text{Fe}_2\text{O}_3]_{\text{F090}}$  to determine the  $[\text{Fe}_2\text{O}_3]_{\text{F090}}$  for a pure melt of the enriched endmember. (B) A simple accumulated fractional melting model is used to relate the inferred primary magmatic  $[\text{Fe}_2\text{O}_3]_{\text{F090}}$  for the depleted (dashed blue line with 95% confidence envelope) and enriched (dashed red line) to that in the source,  $[\text{Fe}_2\text{O}_3]_{\text{source}}$ . Solid thick blue line represents the locus of aggregate melts for a range of source compositions using partition coefficients calculated for a spinel lherzolite (Mallmann and O'Neill, 2009). Thin lines represent how this locus of source composition changes taking endmember cases of melt fraction and partition coefficient values ( $F = 7\text{--}13\%$  and  $D_{\text{Fe}_2\text{O}_3} = 0.1\text{--}0.23$  respectively). Red lines use partition coefficients and melt fractions appropriate to the more fusible garnet-rich pyroxenite lithology inferred to comprise the enriched Icelandic source component (Shorttle and MacLennan, 2011) ( $F = 15\text{--}21\%$  and  $D_{\text{Fe}_2\text{O}_3} = 0.47\text{--}0.64$ ). Vertical grey bars mark the source compositions which, given the assumptions regarding  $F$  and  $D_{\text{Fe}_2\text{O}_3}$ , are consistent with the observed melt compositions. (C) Viable source  $\text{Fe}_2\text{O}_3$  contents are compared to plausible mantle lithologies as black symbols (O'Neill et al., 1993; Lécuyer and Ricard, 1999; Cottrell and Kelley, 2011). White symbols indicate the  $\text{Fe}_2\text{O}_3$  estimated for the enriched Icelandic source, made of equal proportions of primitive upper mantle (PUM) and either fresh MORB or altered oceanic crust (AOC, Shorttle and MacLennan, 2011). (For interpretation of the references to colour in this figure legend, the reader is referred to the web version of this article.)

units. This trend is unlikely to be explained by degassing or crystallisation processes and is the opposite of what would be expected from redox melting of enriched high-carbon mantle domains. Instead, the positive correlation between oxidation and enrichment could reflect the presence of intrinsically oxidised sources in the Icelandic mantle.

Fluid-mobile trace elements are under-enriched in near-plume Reykjanes Ridge basalts with respect to other incompatible elements, given their nominal silicate–melt partition coefficients. In addition to abundant evidence for the presence of recycled material in the Icelandic mantle, the relative under-enrichment of fluid-mobile elements suggests that enriched Icelandic mantle may have been hydrated at a ridge axis, followed by dehydration (and fluid-mobile element loss) during recycling. This ancient ridge axis hydration event, if it happened in the last 600 Ma, will have led to significant oxidation of the oceanic crust. Recycling of this component then introduces trace element-enriched and oxidised material back into the mantle.

By connecting ridge axis oxidation processes to recycling and eventual resampling by mantle plumes, our results are consistent with a role for the solid Earth in long-term oxygen cycling.

### Acknowledgements

OS was supported by a Title A Fellowship from Trinity College, University of Cambridge, JM through NERC grant NE/J021539/1 and MH acknowledges a Junior Research Fellowship from Murray Edwards College, Cambridge. We acknowledge Diamond Light Source for time on beamline I18 under proposals SP9446, SP9456 and SP12130 and the support during our analytical sessions from beamline scientist Konstantin Ignatyev and principal beamline scientist Fred Mosselmans. The Smithsonian Institution National Museum of Natural History is thanked for their loan of NMNH 117393. Charles Langmuir and Liz Cottrell are thanked for their thorough and constructive reviews, their insight greatly improved the

manuscript. Remaining ambiguities and errors are the authors' own.

### Appendix A. Additional figures and tables

**Table A.1**

Step sizes and dwell times used for XANES analysis of the Fe K-edge.

| Energy range (eV) | Step size (eV) | Dwell time (s) |
|-------------------|----------------|----------------|
| 7020.0–7100.0     | 10             | 1              |
| 7101.0–7104.0     | 1.0            | 2              |
| 7104.1–7109.9     | 0.1            | 5              |
| 7110.0–7117.9     | 0.1            | 10             |
| 7118.0–7119.4     | 0.1            | 5              |
| 7119.5–7127.0     | 0.5            | 2              |
| 7128.0–7144.0     | 1.0            | 2              |
| 7148.0–7408.0     | 4.0            | 2              |
| 7410.0–7500.0     | 10             | 1              |

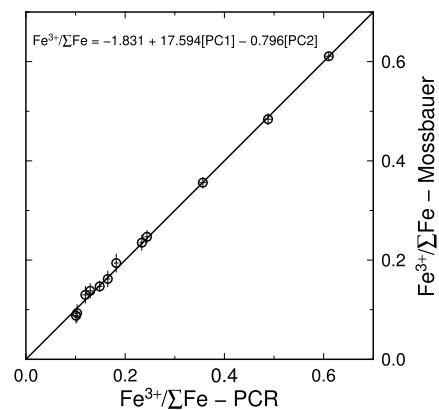


**Fig. A.1.** The result of performing principal component regression (PCR) to take a linear mixture of the first two principal components (Fig. 3) to reconstruct the Mössbauer-derived  $\text{Fe}^{3+}/\Sigma\text{Fe}$ .

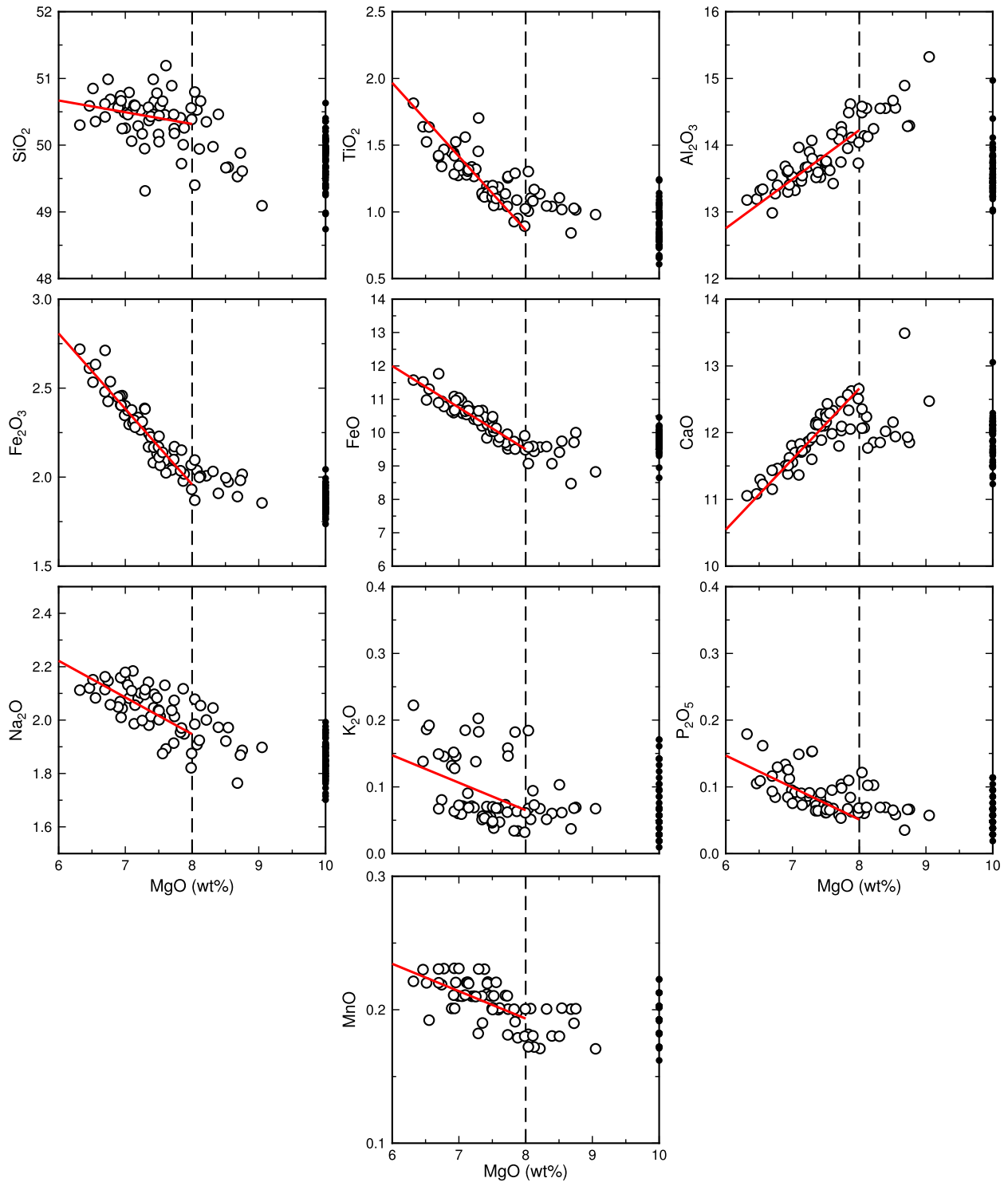


**Fig. A.2.** Plots illustrating how the fractional crystallisation correction has been applied to the data. Samples below 8 wt% MgO first had their MgO content increased to 8 wt%, moving their major element compositions parallel to the red lines in the figures. These lines were calculated by York (1969)-style regression through all the data with MgO < 8 wt%. Subsequent correction to 10 wt% MgO, or  $F_{90}$ , occurred via olivine addition using the Herzberg and O'Hara (2002) olivine model. (For interpretation of the references to colour in this figure legend, the reader is referred to the web version of this article.)

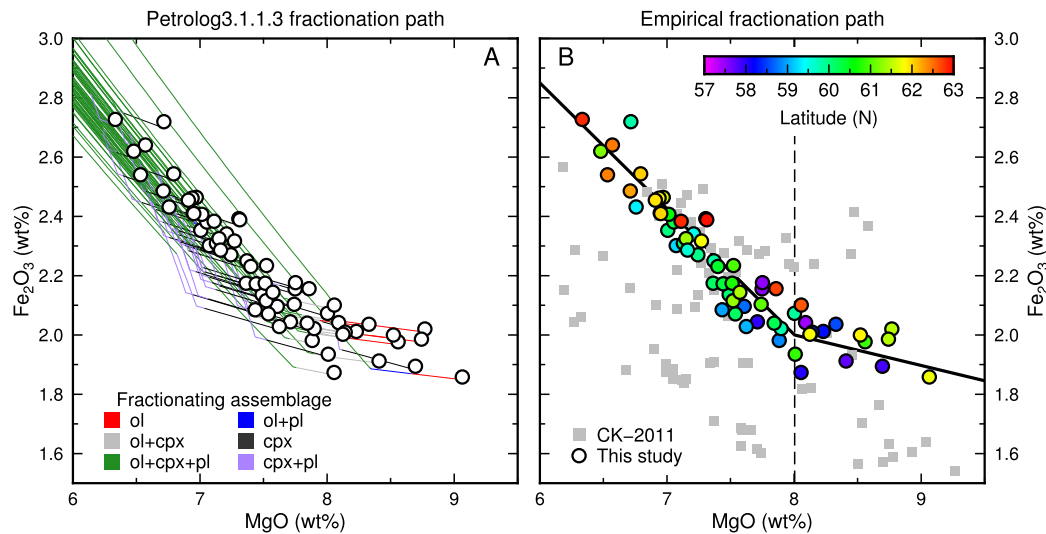


**Fig. A.3.** A comparison between models of fractionation in the Reykjanes Ridge dataset and empirical fits to the data. In (A) Petrolog3 (version 3.1.1.3, Danyushevsky and Plechov, 2011) is used to model fractional crystallisation starting from the major element composition of the sample glasses (open circles) and using the water data of Nichols et al. (2002). Pressure is set to 2 kbar, partition coefficients are  $D_{ol}^{Fe_2O_3} = 0$ ,  $D_{plag}^{Fe_2O_3} = 0$  and  $D_{cpx}^{Fe_2O_3} = 0.45$  (Mallmann and O'Neill, 2009), and we used the mineral–melt models of Herzberg and O'Hara (2002). Fractionation paths are drawn as coloured lines showing the co-crystallising phases. (B) shows the mixed empirical (for samples with  $MgO < 8$  wt%) and model (olivine addition to samples above 8 wt%  $MgO$ ) method of data correction that has been used to construct figures in the main text. Coloured circles are the new data we present here; grey squares are data from Cottrell and Kelley (2011).

**Table A.2**

Covariance and correlation matrices for parameters in the PCR calibration:  $Fe^{3+} / \sum Fe = a_0 + a_1 PC1 + a_2 PC2$ .

|       | Correlation matrix |        |        | Covariance matrix |       |        |
|-------|--------------------|--------|--------|-------------------|-------|--------|
|       | $a_0$              | $a_1$  | $a_2$  | $a_0$             | $a_1$ | $a_2$  |
| $a_0$ | 1.000              | -0.999 | -0.054 | 0.009             | -0.08 | -0.002 |
| $a_1$ | -0.999             | 1.000  | 0.0531 | -0.08             | 0.7   | 0.02   |
| $a_2$ | -0.054             | 0.0531 | 1.000  | -0.002            | 0.02  | 0.2    |

**Table A.3**

Calculated bulk partition coefficients used in modelling for Fig. 10,  $f$  is the fraction of each mineral phase in the source,  $sp$  = spinel,  $gt$  = garnet,  $ol$  = olivine,  $opx$  = orthopyroxene,  $cpx$  = clinopyroxene.

| Lithology         | $f_{sp} D_{sp}$ | $f_{gt} D_{gt}$ | $f_{ol} D_{ol}$ | $f_{opx} D_{opx}$ | $f_{cpx} D_{cpx}$ | $D_{bulk} = \sum f_i D_i$ |
|-------------------|-----------------|-----------------|-----------------|-------------------|-------------------|---------------------------|
| Spinel lherzolite | 0.044           | -               | 0.034           | 0.050             | 0.082             | 0.21                      |
| Spinel pyroxenite | 0.154           | -               | 0.011           | 0.030             | 0.027             | 0.47                      |
| Garnet pyroxenite | -               | 0.27–0.41       | 0.014           | -                 | 0.23              | 0.51–0.65                 |

**Table A.4**

Bulk partition coefficient and melt fraction combinations used in constructing the upper and lower bounds (thin lines) and preferred solution (thick line) for source  $Fe_2O_3$  shown in Fig. 10.  $sp-lrz$  = spinel lherzolite,  $gt-px$  = garnet pyroxenite,  $sp-px$  = spinel pyroxenite.

| Source   | Bound     | Lithology | $D_{bulk}$ | $F$  |
|----------|-----------|-----------|------------|------|
| Depleted | lower     | $sp-lrz$  | 0.1        | 0.07 |
| Depleted | upper     | $sp-lrz$  | 0.23       | 0.13 |
| Depleted | preferred | $sp-lrz$  | 0.21       | 0.1  |
| Enriched | lower     | $sp-px$   | 0.47       | 0.15 |
| Enriched | upper     | $gt-px$   | 0.65       | 0.21 |
| Enriched | preferred | $gt-px$   | 0.51       | 0.18 |

## Appendix B. Supplementary material

Supplementary material related to this article can be found online at <http://dx.doi.org/10.1016/j.epsl.2015.07.017>.

## References

Bajt, S., Sutton, S.R., Delaney, J.S., 1994. X-ray microprobe analysis of iron oxidation states in silicates and oxides using X-ray absorption near edge structure (XANES). *Geochim. Cosmochim. Acta* 58, 5209–5214.

- Ballhaus, C., Frost, B.R., 1994. The generation of oxidised  $CO_2$ -bearing basaltic melts from reduced  $CH_4$ -bearing upper mantle sources. *Geochim. Cosmochim. Acta* 58, 4931–4940.
- Berry, A.J., O'Neill, H.S., Jayasuriya, K.D., Campbell, S.J., Foran, G.J., 2003. XANES calibrations for the oxidation state of iron in silicate glass. *Am. Mineral.* 88, 967–977.
- Bézos, A., Humler, E., 2005. The  $Fe^{3+} / \sum Fe$  ratios of MORB glasses and their implications for mantle melting. *Geochim. Cosmochim. Acta* 69, 711–725.
- Burgisser, A., Scaillet, B., 2007. Redox evolution of a degassing magma rising to the surface. *Nature* 445, 194–197.
- Canfield, D.E., Poulton, S.W., Narbonne, G.M., 2007. Late-Neoproterozoic deep-ocean oxygenation and the rise of animal life. *Science* 315, 92–95.
- Canil, D., O'Neill, H.S.C., Pearson, D.G., Rudnick, R.L., McDonough, W.F., Carswell, D.A., 1994. Ferric iron in peridotites and mantle oxidation states. *Earth Planet. Sci. Lett.* 123, 205–220.
- Carmichael, I.S.E., 1991. The redox states of basic and silicic magmas: a reflection of their source regions? *Contrib. Mineral. Petrol.* 106, 129–141.
- Chase, C.G., 1981. Oceanic island Pb: two-stage histories and mantle evolution. *Earth Planet. Sci. Lett.* 52, 277–284.
- Chauvel, C., Hémond, C., 2000. Melting of a complete section of recycled oceanic crust: trace element and Pb isotopic evidence from Iceland. *Geochim. Geophys. Geosyst.* 1.
- Cottrell, E., Kelley, K.A., 2009. High-precision determination of iron oxidation state in silicate glasses using XANES. *Chem. Geol.* 268, 169–179.
- Cottrell, E., Kelley, K.A., 2011. The oxidation state of Fe in MORB glasses and the oxygen fugacity of the upper mantle. *Earth Planet. Sci. Lett.* 305, 279–282.
- Cottrell, E., Kelley, K.A., 2013. Redox heterogeneity in mid-ocean ridge basalts as a function of mantle source. *Science* 340, 1314–1317.
- Danyushevsky, L.V., Plechov, P., 2011. Petrolog3: integrated software for modeling crystallization processes. *Geochem. Geophys. Geosyst.* 12.
- Dixon, J.E., Clague, D.A., Stolper, E.M., 1991. Degassing history of water, sulfur, and carbon in submarine lavas from Kilauea volcano, Hawaii. *J. Geol.* 99, 371–394.
- Farges, F., Lefrère, Y., Rossano, S., Berthreau, A., Calas, G., Brown Jr., G.E., 2004. The effect of redox state on the local structural environment of iron in silicate glasses: a combined XAFS spectroscopy, molecular dynamics, and bond valence study. *J. Non-Cryst. Solids* 344, 176–188.
- Frost, B.R., 1991. An introduction to oxygen fugacity and its petrological importance. In: Lindsley, D.H. (Ed.), *Oxide Minerals: Petrologic and Magnetic Significance*. In: *Rev. Mineral. Geochem.*, vol. 25. Mineralogical Society of America, Washington, DC, pp. 1–9.
- Gaillard, F., Scaillet, B., Arndt, N.T., 2011. Atmospheric oxygenation caused by a change in volcanic degassing processes. *Nature* 478, 229–232.
- Gibson, S.A., Geist, D., 2010. Geochemical and geophysical estimates of lithospheric thickness variation beneath Galápagos. *Earth Planet. Sci. Lett.* 300, 275–286.
- Hémond, C., Hofmann, A.W., Vlastélic, I., Nauret, F., 2006. Origin of MORB enrichment and relative trace element compatibilities along the Mid-Atlantic Ridge between 10° and 24°N. *Geochim. Geophys. Geosyst.* 7.
- Herzberg, C., O'Hara, M.J., 2002. Plume-associated ultramafic magmas of Phanerozoic age. *J. Petrol.* 43, 1857–1883.

- Hilton, D.R., Thirlwall, M.F., Taylor, R.N., Murton, B.J., Nichols, A., 2000. Controls on the magmatic degassing along the Reykjanes Ridge with implications for the helium paradox. *Earth Planet. Sci. Lett.* 183, 43–50.
- Jones, S.M., Murton, B.J., Fitton, J.G., White, N.J., MacLennan, J., Walters, R.L., 2014. A joint geochemical–geophysical record of time-dependent mantle convection south of Iceland. *Earth Planet. Sci. Lett.* 386, 86–97.
- Jugo, P.J., 2009. Sulfur content at sulfide saturation in oxidized magmas. *Geology* 37, 415–418.
- Kasting, J.F., 2013. What caused the rise of atmospheric O<sub>2</sub>. *Chem. Geol.* 362, 13–25.
- Kelley, K.A., Cottrell, E., 2009. Water and the oxidation state of subduction zone magmas. *Science* 325, 605–607.
- Kessel, R., Schmidt, M.W., Ulmer, P., Pettke, T., 2005. Trace element signature of subduction-zone fluids, melts and supercritical liquids at 120–180 km depth. *Nature* 437, 724–727.
- Kogiso, T., Hirose, K., Takahashi, E., 1998. Melting experiments on homogeneous mixtures of peridotite and basalt: application to the genesis of ocean island basalts. *Earth Planet. Sci. Lett.* 162, 45–61.
- Kress, V.C., Carmichael, I.S.E., 1991. The compressibility of silicate liquids containing Fe<sub>2</sub>O<sub>3</sub> and the effect of composition, temperature, oxygen fugacity and pressure on their redox states. *Contrib. Mineral. Petrol.* 108, 82–92.
- Lécuyer, C., Ricard, Y., 1999. Long-term fluxes and budget of ferric iron: implication for the redox states of the Earth's mantle and atmosphere. *Earth Planet. Sci. Lett.* 165, 197–211.
- Liu, Y., Samaha, N.T., Baker, D.R., 2007. Sulfur concentration at sulfide saturation (SCSS) in magmatic silicate melts. *Geochim. Cosmochim. Acta* 71, 1783–1799.
- Malherbe, J., Clavier, F., 2013. Toward chromium speciation in solids using wave-length dispersive X-ray fluorescence spectrometry Cr K $\beta$  lines. *Anal. Chim. Acta* 773, 37–44.
- Mallmann, G., O'Neill, H.S.C., 2009. The crystal/melt partitioning of V during mantle melting as a function of oxygen fugacity compared with some other elements (Al, P, Ca, Sc, Ti, Cr, Fe, Ga, Y, Zr and Nb). *J. Petrol.* 50, 1765–1794.
- Manceau, A., Gorshkov, A.I., Drits, V.A., 1992. Structural chemistry of Mn, Fe, Co, and Ni in manganese hydrous oxides: Part I. Information from XANES spectroscopy. *Am. Mineral.* 77, 1133–1143.
- McKenzie, D., Stracke, A., Blichert-Toft, J., Albarède, F., Grönvold, K., O'Nions, R.K., 2004. Source enrichment processes responsible for isotopic anomalies in oceanic island basalts. *Geochim. Cosmochim. Acta* 68, 2699–2724.
- Métrich, N., Berry, A.J., O'Neill, H.S., Susini, J., 2009. The oxidation state of sulfur in synthetic and natural glasses determined by X-ray absorption spectroscopy. *Geochim. Cosmochim. Acta* 73, 2382–2399.
- Moussallam, Y., Oppenheimer, C., Scaillet, B., Gaillard, F., Kyle, P., Peters, N., Hartley, M., Berlo, K., Donovan, A., 2014. Tracking the changing oxidation state of Erebus magmas, from mantle to surface, driven by magma ascent and degassing. *Earth Planet. Sci. Lett.* 393, 200–209.
- Murton, B.J., 1995. RSS Charles Darwin Cruise 80, 01 September to 01 October 1993. The PETROS programme: geologic sampling and bathymetric surveying of the Reykjanes Ridge between 57°N and 63°N, southwest of Iceland. Deacon Laboratory Cruise Report 236. Institute of Oceanographic Sciences.
- Murton, B.J., Taylor, R.N., Thirlwall, M.N., 2002. Plume-ridge interaction: a geochemical perspective from the Reykjanes Ridge. *J. Petrol.* 43, 1987–2012.
- Navin, D.A., Sinha, M.C., 1998. The RAMESSES experiment–II. Evidence for accumulated melt beneath a slow spreading ridge from wide-angle refraction and multichannel reflection seismic profiles. *Geophys. J. Int.* 135, 746–772.
- Nichols, A.R.L., Carroll, M.R., Höskuldsson, A., 2002. Is the Iceland hot spot also wet? Evidence from the water contents of undegassed submarine and subglacial pillow basalts. *Earth Planet. Sci. Lett.* 202, 77–87.
- O'Neill, H.S.C., Rubie, D.C., Canil, D., Geiger, C.A., Ross II, C.R., Seifert, F., Woodland, A.B., 1993. Ferric iron in the upper mantle and in transition zone assemblages: implications for relative oxygen fugacities in the mantle. In: *Geophys. Monogr.*, vol. 74. American Geophysical Union, pp. 73–88.
- Press, W.H., Teukolsky, S.A., Vetterling, W.T., Flannery, B.P., 1992. *Numerical Recipes in C*, second edition. Cambridge University Press.
- R Core Team, 2013. *R: A Language and Environment for Statistical Computing*. R Foundation for Statistical Computing, Vienna, Austria.
- Saal, A.E., Hauri, E., Langmuir, C.H., Perfit, M., 2002. Vapour undersaturation in primitive mid-ocean-ridge basalt and the volatile content of Earth's upper mantle. *Nature* 419, 451–455.
- Schilling, J.G., 1973. Iceland mantle plume: geochemical study of Reykjanes ridge. *Nature* 242, 565–571.
- Shorttle, O., MacLennan, J., 2011. Compositional trends of Icelandic basalts: implications for short-lengthscale lithological heterogeneity in mantle plumes. *Geochem. Geophys. Geosyst.* 12.
- Shorttle, O., MacLennan, J., Jones, S.M., 2010. Control of the symmetry of plume ridge interaction by spreading-ridge geometry. *Geochem. Geophys. Geosyst.* 11.
- Shorttle, O., MacLennan, J., Lambert, S., 2014. Quantifying lithological variability in the mantle. *Earth Planet. Sci. Lett.* 395, 24–40.
- Sims, K.W.W., DePaolo, D.J., 1997. Inferences about mantle magma sources from incompatible element concentration ratios in oceanic basalts. *Geochim. Cosmochim. Acta* 61, 765–784.
- Sims, K.W.W., MacLennan, J., Blichert-Toft, J., Mervine, E.M., Blusztajn, J., Grönvold, K., 2013. Short length scale mantle heterogeneity beneath Iceland probed by glacial modulation of melting. *Earth Planet. Sci. Lett.* 379, 146–157.
- Sleep, N.H., 2005. Dioxygen over geologic time. *Met. Ions Biol. Syst.* 43, 49–73.
- Smallwood, J.R., White, R.S., 1998. Crustal accretion at the Reykjanes Ridge, 61°–62°N. *J. Geophys. Res.* 103, 5185–5201.
- Stagno, V., Ojwang, D.O., McCammon, C.A., Frost, D.J., 2013. The oxidation state of the mantle and the extraction of carbon from the Earth's interior. *Nature* 493, 84–88.
- Stracke, A., 2012. Earth's heterogeneous mantle: a product of convection driven interaction between crust and mantle. *Chem. Geol.* 330–331, 274–299.
- Stracke, A., Bizimis, M., Salters, V.J.M., 2003a. Recycling oceanic crust: quantitative constraints. *Geochem. Geophys. Geosyst.* 4.
- Stracke, A., Zindler, A., Salters, V.J.M., McKenzie, D., Blichert-Toft, J., Albarède, F., Grönvold, K., 2003b. Theistareykir revisited. *Geochem. Geophys. Geosyst.* 4.
- Thirlwall, M.F., Gee, M.A.M., Taylor, R.N., Murton, B.J., 2004. Mantle components in Iceland and adjacent ridges investigated using double-spike Pb isotope ratios. *Geochim. Cosmochim. Acta* 68, 361–386.
- Vigneau, E., Devaux, M.F., Qannari, E.M., Robert, P., 1997. Principal component regression, ridge regression and ridge principal component regression in spectroscopy calibration. *J. Chemom.* 11, 239–249.
- White, R.S., Bown, J.W., Smallwood, J.R., 1995. The temperature of the Iceland plume and origin of outward-propagating V-shaped ridges. *J. Geol. Soc. (Lond.)* 152, 1039–1045.
- Wilke, M., Farges, F., Petit, P.E., Brown Jr., G.E., Martin, F., 2001. Oxidation state and coordination of Fe in minerals: an Fe K-XANES spectroscopic study. *Am. Mineral.* 86, 714–730.
- Wilke, M., Jugo, P.J., Klimm, K., Susini, J., Botcharnikov, R., Kohn, S.C., Janousch, M., 2008. The origin of S<sup>4+</sup> detected in silicate glasses by XANES. *Am. Mineral.* 93, 235–240.
- Wong, J., Lytle, F.W., Messmer, R.P., Maylotte, D.H., 1984. K-edge absorption spectra of selected vanadium compounds. *Phys. Rev. B* 30, 5596–5610.
- York, D., 1969. Least squares fitting of a straight line with correlated errors. *Earth Planet. Sci. Lett.* 5, 320–324.